




Competition between subwavelength and deep-subwavelength structures ablated by ultrashort laser pulses

LEI WANG,^{1,†}  BIN-BIN XU,^{2,†} XIAO-WEN CAO,¹ QIAN-KUN LI,¹ WEN-JING TIAN,³ QI-DAI CHEN,^{1,6} SAULIUS JUODKAZIS,^{4,5,7} AND HONG-BO SUN^{1,8}

¹State Key Laboratory on Integrated Optoelectronics, College of Electronic Science and Engineering, Jilin University, Changchun 130012, China

²Centre of Excellence for Quantum Computation and Communication Technology, School of Physics, University of New South Wales, Sydney NSW 2052, Australia

³State Key Laboratory of Supramolecular Structure and Materials, College of Chemistry, Jilin University, Changchun 130012, China

⁴Centre for Micro-Photonics, Faculty of Science, Engineering and Technology, Swinburne University of Technology, Hawthorn VIC 3122, Australia

⁵Melbourne Centre for Nanofabrication, ANFF, 151 Wellington Road, Clayton VIC 3168, Australia

⁶e-mail: chenqd@jlu.edu.cn

⁷e-mail: sjuodkazis@swin.edu.au

⁸e-mail: hbsun@jlu.edu.cn

Received 23 February 2017; revised 20 April 2017; accepted 10 May 2017 (Doc. ID 287410); published 9 June 2017

Femtosecond laser-induced periodic subwavelength and deep-subwavelength structures (SWS; DSWS) have attracted attention due to their subdiffraction resolution of surface and inner volume patterning. Understanding of the richness of laser-matter interaction during formation of SWS and DSWS is another quest which can help to find control for nanoscale fabrication. Lack of control over SWS and DSWS formation has impacted their wider use and calls for a deeper insight into the relationship between them. Herein we present a systematic study defining a criterion for imprinting either SWS or DSWS, which is based on a competition and their mutual incompatibility discriminated by the laser fluence and pulse accumulation. Structure evolution of SWS and DSWS is highly dependent on the localized effective laser fluence, which determines the instantaneous optical permittivity by the laser-excited electrons creating an active plasma layer. The proposed universal SWS and DSWS competition mechanism involving the laser-induced plasma wave at the plasma-substrate interface ties together many previous observations and unifies the discussed mechanisms of surface nanoripple formation. © 2017 Optical Society of America

OCIS codes: (140.3390) Laser materials processing; (320.7130) Ultrafast processes in condensed matter, including semiconductors; (250.5403) Plasmonics; (240.4350) Nonlinear optics at surfaces; (220.4880) Optomechanics.

<https://doi.org/10.1364/OPTICA.4.000637>

1. INTRODUCTION

Laser-induced periodic structures (LIPSS) have been widely reported on surfaces of different materials since their first observation in 1965 on Ge and GaAs irradiated by a ruby laser [1]. Interference between the incident light and the surface-scattered wave was attributed to the structure formation under irradiation by continuous wave and high-power nanosecond and picosecond lasers [2–5]. The period of the formed structure is typically larger than half-wavelength, $\lambda/2$, with a strong dependence on the angle of incidence [4,5]. However, under femtosecond (fs) laser irradiation, periods slightly smaller than the laser wavelength [therefore, sub-wavelength structures (SWS)] [3,4], as well as deep-subwavelength structures (DSWS) [6–11] with periods considerably smaller than $\lambda/2$, were observed on transparent materials and semiconductors. Up to now, these two types of surface structures have become a universally observed feature in the fs laser multipulse ablation

[3–5]. For example, in the case of silicon, SWS with period Λ ranging from 500 to 800 nm ($0.6\lambda < \Lambda \approx \lambda$, $\lambda = 800$ nm) were observed under the amplified fs-laser pulsed exposure [12–20]. DSWS with a period of 70–130 nm ($\Lambda < \lambda/6$, $\lambda = 800$ nm) were realized by a fs-laser oscillator at a several tens of megahertz (MHz) repetition rate [21,22] or by a fs-laser amplifier in solution [17,23,24]. The morphology of SWS or DSWS were nearly the same regardless of the laser parameter differences between repetition rate, incident angle, and pulse duration [4,12,22,25]. However, they were not observed simultaneously on Si by fs-laser exposure using the same wavelength, pulse duration, and repetition rate. Besides, although the modified Sipe's [12,25] and plasmonic wave models [21,24] could provide a self-consistent explanation for the formation of either SWS or DSWS, they cannot consistently encompass formation of both structures. The relation between SWS and DSWS has not been systematically studied.

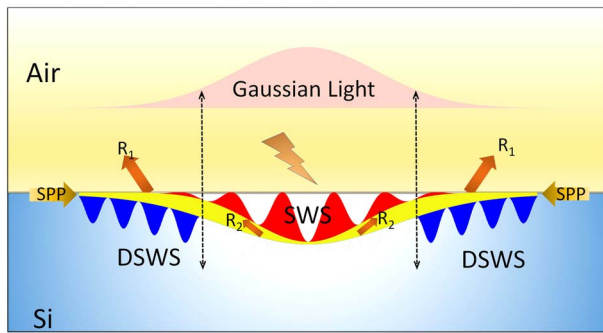


Fig. 1. Laser-induced plasma conductive active layer supporting waves which imprint SWS and DSWS patterns by ablation; surface plasmon polariton (SPP) is formed at the interfaces between the two layers: air-plasma and plasma-substrate. Reflectivity, $R_{1,2}$, and thickness of the plasma layer are varying across the Gaussian focal spot.

Herein, we report on a systematic study of fs-laser-induced SWS and DSWS at different laser fluences from nearly twice the threshold to 1/4 the threshold for structure formation and accumulation with pulse numbers from 1 to 10^5 . The SWS structures were observed above 170 mJ/cm^2 by pulse accumulation, while DSWS were demonstrated between 76 and 170 mJ/cm^2 using the same laser amplifier and washing of the surface in HF acid solution. These two types of structures were found incompatible with each other and strongly dependent on the localized effective laser fluence (ELF)—the actual fluence at the interface on which the structure formed (Fig. 1); the average fluence per laser spot cannot be used to correctly capture formation of the SWS and DSWS. The interface active layer of excited electrons was formed under optical excitation, supporting a plasmonic wave. A near-infrared Ti:sapphire fs laser (Spectra Physics) with repetition rate of 1 kHz was used to maximally suppress thermal accumulation between pulses and to ensure the same average laser fluence used for SWS and DSWS formation. The wavelength of the laser radiation was $\lambda = 800 \text{ nm}$ and pulse duration was 100 fs . Objective lenses ($50\times$ with numerical aperture $\text{NA} = 0.7$ and $10\times$, $\text{NA} = 0.25$) were used to focus the laser beam onto a $\langle 100 \rangle$ silicon surface.

2. COMPETITION BETWEEN SUB- AND DEEP-SUBWAVELENGTH STRUCTURES

The SWS period decreased with the pulse accumulation above the threshold of 230 mJ/cm^2 (Fig. 2). The period was very close to the laser wavelength of 800 nm for the structure recognizable after a single pulse irradiation at the laser fluence of 436 mJ/cm^2 . The period decreased as the pulse number was increasing, and saturated after eight pulses (Fig. 2). This trend was similar for the smaller laser fluence of 344 mJ/cm^2 except that more pulses were required for the same period as compared with 436 mJ/cm^2 . At the laser fluence of 287 mJ/cm^2 , SWS was first observed after 20 pulses with a period of around 660 nm and then kept nearly the same as the pulse number increased. It is worth noting that SWS could be formed by only one pulse at 436 mJ/cm^2 , while ablation appeared before the formation of SWS when the laser fluence was 344 and 287 mJ/cm^2 . The ablation-induced oxidation and material removal affected the final appearance of the structure but was not an essential prerequisite for the SWS formation. Ablation

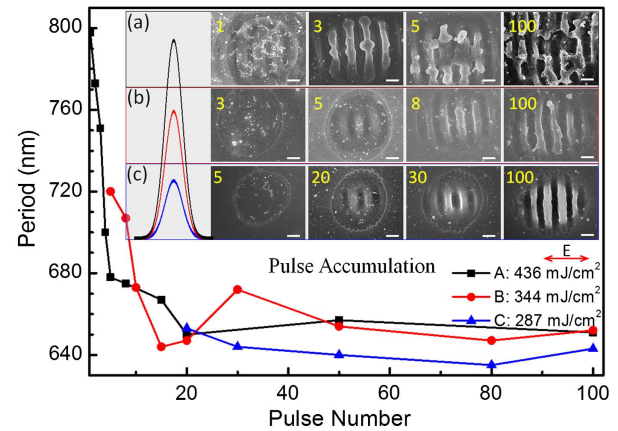


Fig. 2. Period of SWS versus pulse accumulation at different laser fluences. Representative SEM images at different laser fluences of (a) 436 mJ/cm^2 , (b) 344 mJ/cm^2 , and (c) 287 mJ/cm^2 shown as inset figures. Numbers in left upside of each inset figure represent the number of laser pulses. All scale bars are 500 nm . Arrow shows the laser polarization.

was enhanced by a positive feedback due to the light scattering from periodic structures and at the ablation rim. Periodicity of pattern was damaged and holes formed at the center of the irradiation spot when the number of pulses exceeded 10^2 . All the structures were analyzed after HF acid etching (5 mol/L) for 15 min to remove the oxidation and the ablation debris.

A serrated edge of focal region became more obvious and developed DSWS at the fluence of 258 mJ/cm^2 ; see Fig. 2 and condition C in Fig. 3. At first, some melting and nanoparticles were only observed in the ablation center after single-pulse ablation

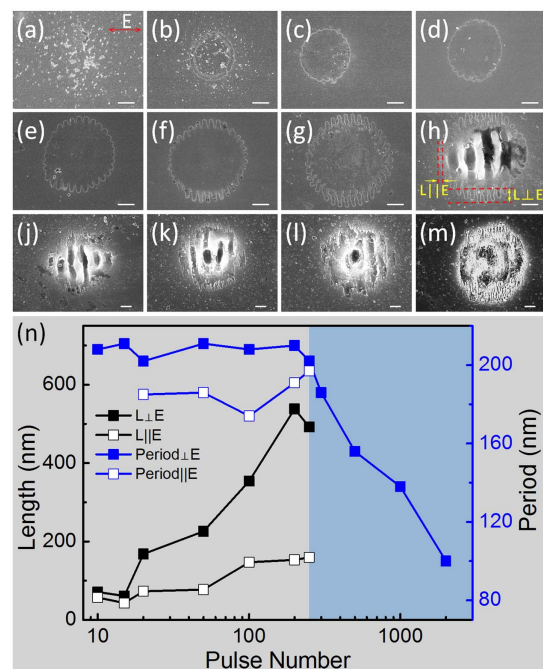


Fig. 3. SWS (filled markers) and DSWS (open) evolution with pulse accumulation at laser fluence of 258 mJ/cm^2 . Pulse number is (a) 1, (b) 5, (c) 10, (d) 20, (e) 50, (f) 100, (g) 200, (h) 250, (j) 300, (k) 500, (l) 1000, and (m) 2000. The maximum length and period of DSWS. Scale bar for (a)–(m) denotes 500 nm .

[Fig. 3(a)]. They gradually formed a round border after five pulses [Fig. 3(b)]. Then the surface morphology showed a similar serrated rim for 10–20 pulses as that observed after five pulses at the laser fluence of 287 mJ/cm² [Figs. 3(c) and 3(d)]. Interestingly, the period and the length of DSWS grew with pulse number.

Orientation of DSWS was preferentially along the laser polarization. The DSWS formed at the rim of the laser ablation region were about 60 and 70 nm after 20 pulses in the direction parallel to the laser polarization, as shown in Figs. 3(g) and 3(h). They extended outside up to 500 nm at 250 pulses along the polarization; however, there was a clear tendency to observe also DSWS which are perpendicular to the polarization [Fig. 3(h) and 3(m)]. The period of DSWS showed a constant value as the number of pulses increased, 210–10 nm in the direction perpendicular to the laser polarization and 190–10 nm parallel to the polarization [Fig. 3(m)]. If more than 250 pulses were irradiated, DSWS perpendicular the laser polarization were decreasing in period from 200 nm at 300 pulses to about 100 nm at 2000 pulses, while the DSWS in the other direction (parallel to polarization) rapidly disappeared. At the same time, SWS with period about 580–40 nm were clearly observed in the center of the ablation region only when 250 pulses were irradiated, as shown in Fig. 3(h). It kept this period value when the number of pulses was increasing from 300 to 500 and become irregular for the higher pulse number due to a strong light scattering, as shown in Fig. 3(m). All the structures were rinsed in HF acid solution (5 mol/L) for 15 min to remove the oxidation and the ablation fragments before structural characterization by scanning electron microscopy (SEM).

Next, we analyzed SWS and DSWS obtained simultaneously at the irradiated spot. The atomic force microscope (AFM; iCON, Veeco) image of the formed DSWS by 100 pulses at 258 mJ/cm² is shown in Fig. 4(a). The height of the DSWS around the ablation rim and at the center was about 40 nm and slightly increased to 48 nm at 300 pulses [Fig. 4(b)]. The height of the SWS was more than 150 nm at 300 pulses in the center of the ablation pit. More details were revealed by

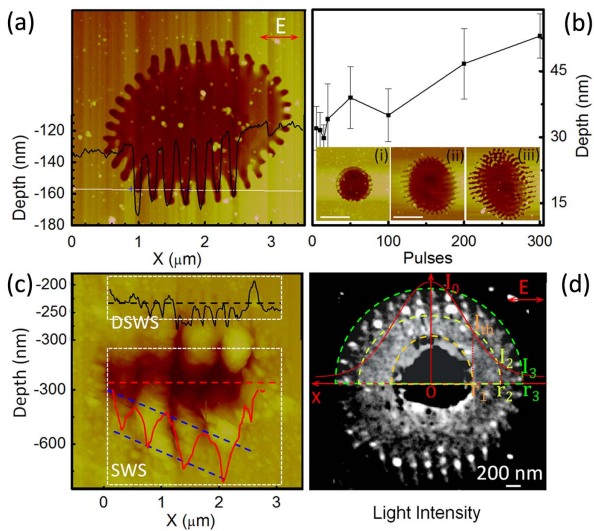


Fig. 4. (a) DSWS formed by 100 pulses at 258 mJ/cm². (b) Depth of DSWS changed with pulse number. (c) SWS formed by 300 pulses at 258 mJ/cm². (d) Laser fluence distribution on the same structure before HF etching (SEM image).

comparing the ablation region before and after HF rinse (Fig. 4). Only a slight signature of DSWS was observed along the polarization between the yellow and green ovals [Fig. 4(d)]. Rinsing in HF revealed the hidden structures by dissolving the oxidation region and by removing ablation debris. The ablated features at the very rim of the pattern have orientation along the laser polarization [Fig. 3(h)] and are consistent with an increased electronic conductivity along the E-field of light during the pulse [26].

Next, formation of SWS and DSWS is investigated by analysis of the light-induced permittivity changes that result in different plasma densities as revealed in experiments (schematically shown in Fig. 1). The critical laser intensity for DSWS formation was defined for the Gaussian light intensity by

$$I_{th,2,3} = I_0 \exp(-2r_{th,2,3}^2/\omega^2), \quad (1)$$

where I_0 is the intensity amplitude at the center, I_{th} is the threshold of laser ablation, I_2 is the upper limit intensity for DSWS formation, I_3 is the lower intensity bound for DSWS, and w is the waist of the beam (radius). Following the relationship between the intensity I and fluence F [27], the critical threshold for DSWS can be estimated between $F(r_3)$ and $F(r_2)$ by defining $\gamma_{12} = r_1^2/r_2^2$ and $\gamma_{13} = r_1^2/r_3^2$:

$$I(t) = I_0 e^{-(t/t_0)^2}, \quad (2)$$

$$F = \int_{-\infty}^{+\infty} I(t) dt = I_0 \int_{-\infty}^{+\infty} e^{-(t/t_0)^2} dt = \sqrt{\pi} t_0 I_0, \quad (3)$$

$$F(r) = F_{th}^\gamma / F_0^{1-\gamma}, \quad (4)$$

with $r_1 = 0.45 \mu\text{m}$, $r_2 = 0.95 \mu\text{m}$, $r_3 = 1.38 \mu\text{m}$, $F(r_2)$ and $F(r_3)$ were found to be at 154 mJ/cm² and 87 mJ/cm², respectively [Fig. 4(d)], and t_0 is the pulse duration. Structures formed at the subthreshold (for a single pulse) laser ablation are shown in Fig. 5. Only DSWS without SWS were observed at 152 mJ/cm² for the pulse accumulation from 1 to 10⁵ as expected from the established threshold. The period 100 ± 10 nm was determined for 10⁴ pulses and then increased to 110 ± 15 nm for larger number of pulses, as shown in Fig. 5. Due to a slight jitter of laser fluence, SWS or an unstructured ablation pit randomly appeared at the fluence of 170 mJ/cm² for 10³ pulses

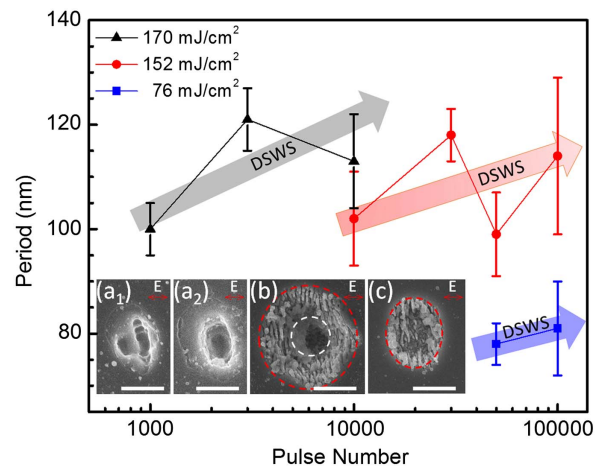


Fig. 5. DSWS formed by subthreshold laser fluence. (a₁–a₂) Structures ablated by 10³ pulses at fluence of 170 mJ/cm². (b)–(c) Structures ablated by 152 mJ/cm² and 76 mJ/cm² by 10⁵ pulses. Scale bar in the insets is 1 μm.

(Fig. 5). The fluence 170 mJ/cm^2 was determined as the lower limit for the SWS formation. A low threshold for the SWS becomes 76 mJ/cm^2 for an increased number of pulses (Fig. 5).

3. CRITERION OF SUB- AND DEEP-SUBWAVELENGTH STRUCTURES BY EFFECTIVE LASER FLUENCE

The photo-excited carrier concentration via absorption and ionization plays a key role in the SWS and DSWS formation. A surface layer where the strongest absorption takes place is changing its effective dielectric permittivity instantaneously following the optical energy deposition. This skin plasma layer supports a plasmonic surface wave (Fig. 1). Considering the indirect and direct energy gap of silicon at 1.12 eV and 3.4 eV, respectively, single-photon ionization (SPI) and two-photon ionization (TPI) are probable at the 800 nm central wavelength excitation. The single- and two-photon ionization created the laser-induced carrier concentration, N_{ch} , which was calculated following the standard definitions and parameters of Si [27],

$$N_{\text{ch}} = N_{\text{SPI}} + N_{\text{TPI}} \quad (5)$$

with

$$N_{\text{SPI}} = \alpha F_0 \frac{1-R}{\hbar \omega}, \quad (6)$$

$$N_{\text{TPI}} = \frac{\beta F_0^2 (1-R)^2}{\hbar \omega 2\sqrt{2\pi} t_0}, \quad (7)$$

where β is the two-photon absorption (TPA) and α is the linear absorption coefficients, respectively; and R is the reflection coefficient. The excited carrier concentration altered effective dielectric permittivity ϵ^* of the active plasma layer is given by [27]

$$\epsilon^* = 1 + (\epsilon_d - 1) \frac{N_0 - N_{\text{ch}}}{N_0} - \frac{\omega_p^2}{\omega^2} \frac{1}{1 + i(\omega \tau_D)^{-1}}, \quad (8)$$

$$\epsilon_d = (n_{\text{Si}} + k_{\text{Si}})^2, \quad \omega_p = \sqrt{\frac{N_e e^2}{\epsilon_0 m^*}}, \quad (9)$$

where n_{Si} and k_{Si} are the real and imaginary parts of the refractive index of Si at 800 nm, defined by $3.681 + 0.005i$; ω and ω_p are the cyclic and plasma frequencies, respectively; e is the electron charge, $1.6 \times 10^{-19} \text{ C}$; ϵ_0 is the vacuum permittivity, $8.854 \times 10^{-12} \text{ F/m}$; m^* is the effective electron mass, 0.18 [27]; and τ_D is the damping time constant, 1 fs [27].

Considering the two plasmonic surface plasmon polariton (SPP) waves formed on the different interfaces between the air-plasma and plasma-substrate (Fig. 1), the effective dielectric constant for each is

$$\frac{1}{\epsilon} = \frac{1}{\epsilon^*} + \frac{1}{\epsilon_s}, \quad (10)$$

where ϵ_s represents the dielectric constant of the environment and dynamically varies as a function of the air, an oxidized film on Si (see the Supplement 1, Fig. S3), and the bulk silicon. The proportion of these different components in the effective medium varies as ablation develops under pulse accumulation. The value of ϵ_s at the upper and lower surfaces is defined by the effective medium formalism applicable due to the subwavelength structure,

$$\epsilon_{s1} = f(\epsilon_{\text{SiO}_2}, \epsilon_{\text{Air}}) = x\epsilon_{\text{Air}} + (1-x)\epsilon_{\text{SiO}_2}, \quad (11)$$

$$\epsilon_{s2} = f(\epsilon_{\text{Si}}, \epsilon_{\text{SiO}_2}) = x\epsilon_{\text{Si}} + (1-x)\epsilon_{\text{SiO}_2}, \quad (12)$$

where the $\epsilon_{\text{air}} = 1$ and the $\epsilon_{\text{SiO}_2} = 2.3$. For the structures with well-defined boundaries, x was taken as the grating width-to-period ratio for both SWS and DSWS.

The effective complex refractive index, $n_e + ik_e$, was defined by

$$\epsilon = \frac{\epsilon^* + \epsilon_s}{\epsilon^* \epsilon_s} = (n_e + ik_e)^2. \quad (13)$$

Interference of the incident and light scattered from the surface based on Sipe's model was attributed to the normal-perpendicular to the linear polarization—SWS formation with period [4,12,17]

$$\Lambda = \lambda/n_e. \quad (14)$$

The normal DSWS were attributed to the plasmonic wave with period [4,21]

$$\Lambda_{\text{DSWS}} = \lambda_{\text{sp}}/2, \quad (15)$$

where the wavelength of SPP λ_{sp} is dependent on the plasma density (hence permittivity) and is defined by

$$\lambda_{\text{sp}} = \frac{2\pi}{k_{\text{sp}}} = \frac{2\pi c}{\omega n_e} = \frac{\lambda}{n_e}. \quad (16)$$

It should be noted the instantaneous reflection at the two interfaces is changing with absorption for the two interfaces (Fig. 1),

$$R_1 = \frac{(n_e - 1)^2 + k_e^2}{(n_e + 1)^2 + k_e^2}, \quad (17)$$

$$R_2 = \frac{(n_e - n_{\text{Si}})^2 + k_{\text{Si}}^2}{(n_e + n_{\text{Si}})^2 + k_{\text{Si}}^2}. \quad (18)$$

The laser fluence changed due to the reflection at the air-plasma interface is

$$F_1 = F_0(1 - R_1). \quad (19)$$

In order to estimate the effective absorbance at the lower interface, the transmittance of the plasma layer should be taken into account,

$$F_2 = F_1 R_2 = F_0(1 - R_1)R_2. \quad (20)$$

By using Eqs. (5)–(8), the N_{SPI} , N_{TPI} , and the total excited electron concentration N_{ch} with laser fluence were iteratively calculated [Fig. 6(a)]. The linear and TPA mechanisms had contribution in electron excitation, plasma layer formation, and, hence, in the final structure formation, which is a result of ablation (imprint) of the SPP waves. From simulation, the threshold of surface structure formation was judged from the lowest reflection, which was at about 219 mJ/cm^2 , close to the experimental observation, 230 mJ/cm^2 , and existing literature, 200 mJ/cm^2 [13,23]. As the laser fluence increased reaching the threshold, the reflection from the interfaces between the air and plasma layer decreased from 0.32 to 0.2. Above the threshold, the reflectivity at the interface between the active layer and the bulk silicon increased quickly with the increasing fluence [Fig. 6(a)]. Such reflectivity changes ensured a stable energy absorption inside the active plasma layer important for the SWS and DSWS formation.

As shown in Fig. 6(b), the SWS period calculated by Eq. (16) presented a stable period of about 780 nm, while the DSWS period was around 100 nm, given by Eq. (17). Although the theoretical fluence for the stable period of SWS and DSWS were

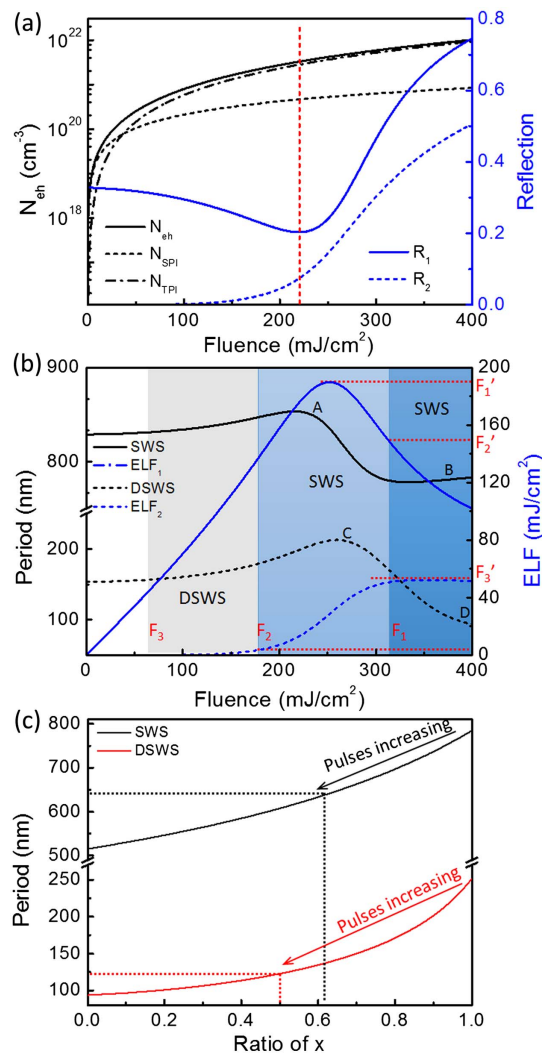


Fig. 6. Laser fluence determined a structure via formation the plasmonic active layer. (a) Excited electron concentration and reflection versus laser fluence. (b) Induced SWS ($x = 1$) and DSWS ($x = 1$) period and the corresponding effective laser fluence (ELF). (c) SWS and DSWS period with x .

nearly the same, $F_1 = 315$ mJ/cm 2 , the effective fluence, which differed across the laser spot, was the key factor that determined which structures could be formed (Fig. 1). When the laser fluence was above F_1 , the excited electron concentration was enough to ensure a stable period for SWS, even by only one laser pulse [Fig. 2(a)]. Nevertheless, the $F'_2 = 147$ mJ/cm 2 was required to form the active plasma layer [right axis on Fig. 6(b)], which means that the fluence below F_1 but above F'_2 was required to generate the same active plasma layer supporting the scattered surface wave and the interference between it and the incident light for the standard SWS according to Sipe's theory. Due to the changed surface reflectivity during pulse accumulation, the experimentally observed lower limit fluence for SWS F_2 was $F'_2/(1 - 0.2) = 184$ mJ/cm 2 , which was in a good agreement with the experimental result of 170 mJ/cm 2 (Fig. 5). For DSWS, the required calculated fluence was only $F'_3 = 52$ mJ/cm 2 , which means the experimentally observed lower limit at the fluence F_3 , which was $F'_3/(1 - 0.2) = 65$ mJ/cm 2 , was close to the experimental result of 76 mJ/cm 2 . Thus, the criterion between

the SWS and DSWS is clearly defined, and correspondence between simulations and experiment was good for the F_2 and F_3 , shown in Fig. 6(b) and schematically in Fig. 1.

Pulse accumulation is the key factor allowing the excited carrier concentration to reach the required high plasma density for SWS and DSWS formation, which was reflected by the evolution of period and the volume ratio x . The $x = 1$ for SWS and $x \lesssim 1$ for DSWS represents the initial air–dielectric boundary, for which the period obtained by simulations were 785 nm for SWS and 210 nm for DSWS [Fig. 6(c)], which were close to the experimental values of 798 ± 7 nm [436 mJ/cm 2 in Fig. 2(a)] and 210–10 nm [Fig. 3(n)], respectively. Due to a slight decrease of the surface dielectric constant [Eqs. (13) and (14)], once the electron concentration is enough to support a stable surface wave, the period of SWS kept a saturated value shown in Fig. 6(b) in agreement with experiments (Fig. 2). The DSWS period would slightly increase with the laser fluence or pulse accumulation; see simulation in Supplement 1, Fig. S4 and experimental data in Fig. 5.

Due to the Gaussian distribution of light intensity, the depth of the active layer became likewise Gaussian as shown in Fig. 1. At the border of the ablation pit, the active layer thickness defined by the plasma skin depth resulted in the same depth of the formed DSWS (see Supplement 1 Fig. S1 and Fig. 1). The depth of the active plasma layer was thinner at the bottom of the center of the ablation pit (Fig. 1 and Supplement 1, Fig. S1). In the center, SWS were dominating on the very thin active plasma layer and prevented the DSWS formation at the plasma–substrate interface (Figs. 2 and 3). Such a competition model of SWS above the skin layer and DSWS below the skin layer was also confirmed by comparing the pulse accumulation at 3000 pulses before and after etching (Supplement 1, Fig. S2).

In summary, we have demonstrated fs-laser-induced subwavelength and deep-subwavelength structures on silicon, and showed the criterion which discriminated formation of these two types of surface structures. We analyzed the laser excitation process and formation of an active plasma layer of the excited electrons, which supported a SPP surface wave. It was established that the effective laser fluence has to be considered and local light fluence is responsible for the formation of SWS and DSWS. The self-consistent relation between SWS and DSWS via modeling of the laser-induced plasma layer at the interfaces ties together previous observations and unifies the mechanisms for surface nanoripple formation.

Funding. National Basic Research Program of China (973 program) (91323301, 91423102, 61590930, 61435005, 51335008); Australian Research Council (ARC) (DP170100131 Discovery project); Changjiang Scholar Program of Chinese Ministry of Education.

Acknowledgment. SJ is grateful for the Chiangjiang scholar grant, which supported a research stay at Jilin University.

*These authors contributed equally for this work.

See Supplement 1 for supporting content.

REFERENCES

1. M. Birnbaum, "Semiconductor surface damage produced by Ruby laser," J. Appl. Phys. **36**, 3688–3689 (1965).

2. J. E. Sipe, J. F. Young, J. S. Preston, and H. M. van Driel, "Laser-induced periodic surface structure, I: theory," *Phys. Rev. B* **27**, 1141–1154 (1983).
3. J. Bonse and A. Rosenfeld, "Femtosecond laser-induced periodic surface structures: recent approaches to explain their sub-wavelength periodicities," *Proc. SPIE* **7994**, 79940M (2010).
4. R. Buividas, M. Mikutis, and S. Juodkazis, "Surface and bulk structuring of materials by ripples with long and short laser pulses: recent advances," *Prog. Quantum Electron.* **38**, 119–156 (2014).
5. D. Tan, K. N. Sharafudeen, Y. Yue, and J. Qiu, "Femtosecond laser induced phenomena in transparent solid materials: fundamentals and applications," *Prog. Mater. Sci.* **76**, 154–228 (2016).
6. Y. Shimotsuma, P. G. Kazansky, J. Qiu, and K. Hirao, "Self-organized nanogratings in glass irradiated by ultrashort light pulses," *Phys. Rev. Lett.* **91**, 247405 (2003).
7. S. Hohm, A. Rosenfeld, J. Krüger, and J. Bonse, "Femtosecond diffraction dynamics of laser-induced periodic surface structures on fused silica," *Appl. Phys. Lett.* **102**, 054102 (2013).
8. J. Liu, T. Jia, K. Zhou, D. Feng, S. Zhang, H. Zhang, X. Jia, Z. Sun, and J. Qiu, "Direct writing of 150 nm gratings and squares on ZnO crystal in water by using 800 nm femtosecond laser," *Opt. Express* **22**, 32361–32370 (2014).
9. S. Wang, G. Feng, and S. Zhou, "Microsized structures assisted nanostructure formation on ZnSe wafer by femtosecond laser irradiation," *Appl. Phys. Lett.* **105**, 253110 (2014).
10. L. Wang, Q. D. Chen, R. Yang, B. B. Xu, H. Y. Wang, H. Yang, C. S. Huo, H. B. Sun, and H. L. Tu, "Rapid production of large-area deep sub-wavelength hybrid structures by femtosecond laser light-field tailoring," *Appl. Phys. Lett.* **104**, 031904 (2014).
11. Y. Liao, J. Ni, L. Qiao, M. Huang, Y. Bellouard, K. Sugioka, and Y. Cheng, "High-fidelity visualization of formation of volume nanogratings in porous glass by femtosecond laser irradiation," *Optica* **2**, 329–334 (2015).
12. J. Bonse, A. Rosenfeld, and J. Krüger, "On the role of surface plasmon polaritons in the formation of laser-induced periodic surface structures upon irradiation of silicon by femtosecond laser pulses," *J. Appl. Phys.* **106**, 104910 (2009).
13. J. Bonse, A. Rosenfeld, and J. Krüger, "Femtosecond laser-induced periodic surface structures: recent approaches to explain their sub-wavelength periodicities," *Proc. SPIE* **7994**, 79940M (2011).
14. J. Bonse, J. Krüger, S. Höhm, and A. Rosenfeld, "Femtosecond laser-induced periodic surface structure," *J. Laser Appl.* **24**, 042006 (2012).
15. G. D. Tsibidis, M. Barberoglou, P. A. Loukakos, E. Stratakis, and C. Fotakis, "Dynamics of ripple formation on silicon surfaces by ultrashort laser pulses in subablation conditions," *Phys. Rev. B* **86**, 115316 (2012).
16. L. Jiang, W. Han, X. Li, Q. Wang, F. Meng, and Y. Lu, "Crystal orientation dependence of femtosecond laser-induced periodic surface structure on (100) silicon," *Opt. Lett.* **39**, 3114–3117 (2014).
17. R. Kuladeep, C. Sahoo, and D. Narayana Rao, "Direct writing of continuous and discontinuous sub-wavelength periodic surface structures on single-crystalline silicon using femtosecond laser," *Appl. Phys. Lett.* **104**, 222103 (2014).
18. J. Song, J. Ye, X. Lin, Y. Dai, G. Ma, H. Li, Y. Jiang, and J. Qiu, "Discussion of the possible formation mechanism of near-wavelength ripples on silicon induced by femtosecond laser," *Appl. Phys. A* **118**, 1119–1125 (2015).
19. W. Han, L. Jiang, X. Li, Y. Liu, and Y. Lu, "Femtosecond laser induced tunable surface transformations on (111) Si aided by square grids diffraction," *Appl. Phys. Lett.* **107**, 251601 (2015).
20. G. D. Tsibidis, C. Fotakis, and E. Stratakis, "From ripples to spikes: a hydrodynamical mechanism to interpret femtosecond laser-induced self-assembled structures," *Phys. Rev. B* **92**, 041405 (2015).
21. M. Straub, M. Afshar, D. Feili, H. Seidel, and K. Koenig, "Periodic nanostructures on Si(100) surfaces generated by high-repetition rate sub-15 fs pulsed near-infrared laser light," *Opt. Lett.* **37**, 190–192 (2012).
22. R. Le Harzic, H. Schuck, D. Sauer, T. Anhut, I. Riemann, and K. König, "Sub-100 nm nanostructuring of silicon by ultrashort laser pulses," *Opt. Express* **13**, 6651–6656 (2005).
23. C. Wang, H. Huo, M. Johnson, M. Shen, and E. Mazur, "The thresholds of surface nano-/micro-morphology modifications with femtosecond laser pulse irradiations," *Nanotechnology* **21**, 75304 (2010).
24. T. J.-Y. Derrien, R. Koter, J. Krüger, S. Höhm, A. Rosenfeld, and J. Bonse, "Plasmonic formation mechanism of periodic 100-nm-structures upon femtosecond laser irradiation of silicon in water," *J. Appl. Phys.* **116**, 074902 (2014).
25. M. Huang, F. Zhao, Y. Cheng, N. Xu, and Z. Xu, "Origin of laser-induced near-subwavelength ripples: interference between surface plasmons and incident laser," *ACS Nano* **3**, 4062–4070 (2009).
26. S. Rekštytė, T. Jonavičius, D. Gailevičius, M. Malinauskas, V. Mizeikis, E. G. Gamaly, and S. Juodkazis, "Nanoscale precision of 3D polymerization via polarization control," *Adv. Opt. Mater.* **4**, 1209–1214 (2016).
27. K. Sokolowski-Tinten and D. von der Linde, "Generation of dense electron-hole plasmas in silicon," *Phys. Rev. B* **61**, 2643–2650 (2000).